



## T-cell movement on the reticular network

Graham M. Donovan<sup>a,\*</sup>, Grant Lythe<sup>b</sup>

<sup>a</sup> Department of Mathematics, University of Auckland, Private Bag 92019, Auckland 1142, New Zealand

<sup>b</sup> Department of Applied Mathematics, University of Leeds, LS2 9JT, UK

### ARTICLE INFO

#### Article history:

Received 16 August 2010

Received in revised form

30 October 2011

Accepted 1 November 2011

Available online 12 November 2011

#### Keywords:

FRC network

Stromal network

Random walk

Brownian motion

*in vivo* Imaging

### ABSTRACT

The idea that the apparently random motion of T cells in lymph nodes is a result of movement on a reticular network (RN) has received support from dynamic imaging experiments and theoretical studies. We present a mathematical representation of the RN consisting of edges connecting vertices that are randomly distributed in three-dimensional space, and models of lymphocyte movement on such networks including constant speed motion along edges and Brownian motion, not in three-dimensions, but only along edges. The simplest model, in which a cell moves with a constant speed along edges, is consistent with mean-squared displacement proportional to time over intervals long enough to include several changes of direction. A non-random distribution of turning angles is one consequence of motion on a preformed network. Confining cell movement to a network does not, in itself, increase the frequency of cell–cell encounters.

© 2011 Elsevier Ltd. All rights reserved.

### 1. Introduction

The adaptive immune response depends on T cells coming into physical contact with antigen-presenting cells (APCs) in the T cell zone of one of the body's lymph nodes (Miller et al., 2004a; Hugues et al., 2004; Celli et al., 2005; Bajénoff et al., 2007; Bousso, 2008). Recent advances in imaging techniques, especially two-photon microscopy, have enabled direct observation of the movement of labelled cells in the lymph nodes of living mice (Miller et al., 2002, 2004b; Stoll et al., 2002; Beauchemin et al., 2007; Millington et al., 2007; Garside and Brewer, 2008; Bousso et al., 2002). A large body of experimental evidence and analysis of the trajectories of individual cells indicate that their paths are consistent with an underlying random process: plotting the mean-squared displacement against time yields a straight line, as would be found if cells underwent Brownian motion, in a range of time intervals from several minutes to an hour (Miller et al., 2002; Wei et al., 2003; Catron et al., 2004; Sumen and Mempel, 2004; Meyer-Hermann and Maini, 2005; Zinselmeyer et al., 2005; Woolf et al., 2007; Beauchemin et al., 2007; Riggs et al., 2008; Worbs and Förster, 2009).

It has recently been proposed that, rather than exploring three-dimensional space, T cells move on the network that fills the T-cell zone of the lymph node known as the *reticular network* (RN) (Katakai et al., 2004; Kaldjian et al., 2001; Gretz et al., 1997;

Ushiki et al., 1995). The RN contains fibroblastic reticular cells (FRCs) (Bajénoff et al., 2006, 2008; Beauchemin et al., 2007; Mueller and Ahmed, 2008; Mueller and Germain, 2009) and may be referred to as the FRC network or stromal network. It has also been reported that the RN acts as a conduit system, transporting soluble antigen to resident dendritic cells (Sixt et al., 2005), and that FRCs secrete the T cell survival factor interleukin-7 (Link et al., 2007). There is experimental evidence, from combinations of imaging techniques, that T lymphocytes and thymocytes migrate in contact with FRCs and that their changes of direction are correlated with branches in RNs (Bajénoff et al., 2006, 2008; Sanos et al., 2011).

A number of models of lymphocyte movement exist in the literature, generally considering free movement in space (Worbs and Förster, 2009; Beltman et al., 2007a; Grigorova et al., 2010; Textor et al., 2011), and sometimes with the idea of movement on a network in mind (Preston et al., 2006; Beltman et al., 2007b; Bogle and Dunbar, 2008). For example, Beauchemin et al. (2007) use three parameters: free speed, free run time and pause time, where cells crawl for the free run time at the free speed, and then pause before heading in a new direction chosen from a density of turning angles. This model exhibits a characteristic two-regime behaviour in mean displacement as a function of time. Beltman et al. (2007b) employ the Potts model on a lattice, explicitly following cell shapes and interactions. Bogle and Dunbar (2008) use an agent-based model on a packed lattice, and Preston et al. (2006) a transport-limited chemical reaction. Grigorova et al. (2010) consider a series of periods of straight-line movement with the possibility of correlations between successive directions.

\* Corresponding author. Tel.: +64 9 373 7599; fax: +64 9 373 7457.

E-mail addresses: [g.donovan@auckland.ac.nz](mailto:g.donovan@auckland.ac.nz) (G.M. Donovan), [grant@maths.leeds.ac.uk](mailto:grant@maths.leeds.ac.uk) (G. Lythe).

Here, we take a different approach by first explicitly constructing the RN network, and then confining all cell motion to it.

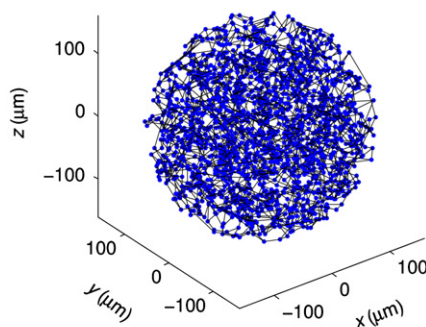
The first step in constructing a computational model of motion on the RN is the construction of the network itself. One must define a set of vertices and edges joining the vertices. We assume each vertex in the network is connected to exactly three edges, motivated by the idea that a vertex is formed when a growing fibre branches into two. The second step is to define the rules of cell motion on this network. We consider different hypotheses for the motion of cells along edges of the network, and rules governing the direction chosen at vertices. The properties of cell paths depend on these rules as well as on the properties of the network itself.

We also explore the implications of RN-based motion for encounters between APCs and T-cells. Because some dendritic cells reside on the network (Lämmermann and Sixt, 2008), restricting T cell motion to a network may be envisaged as a mechanism for bringing about T cell-dendritic cell encounters more efficiently (Charnick and Lauffenburger, 1990). However, we find that motion confined to the network does not increase the frequency of encounters, compared to the frequency of encounters of cells following Brownian motion in three-dimensional space.

## 2. Network model

### 2.1. Constructing the network

Our spatial random networks (Deijfen, 2009; Holroyd et al., 2009) are constructed by first positioning vertices at random, by sampling from the uniform distribution, and then generating edges between them. The position of each of the  $N$  vertices is independently drawn from the uniform distribution inside a sphere of radius  $R$ , so that the density of vertices is  $\rho = 3N/4\pi R^3$ . Connecting the set of vertices with edges is done in two stages. In the first stage, a randomly-chosen vertex,  $n_1$ , is connected to its nearest neighbour, denoted  $n_2$ ;  $n_2$  is connected to  $n_3$ , where  $n_3$  is the nearest vertex to  $n_2$  that is not yet connected, and the process is continued until  $n_{N-1}$  is connected to  $n_N$ . In the second stage,  $N-1$  vertices are picked without replacement from the set of  $N$ , and for each vertex an edge is created joining it to the nearest vertex that it is not already connected to and has fewer than three edges. In this way, a random network is generated with a known number of vertices, uniformly distributed in space, each connected to three other vertices. The network thus constructed does not divide into non-communicating subsets; a path exists between any two vertices of the network, although the shortest path may pass through many other vertices.



In Fig. 1, we display a small sample network and a plot of the mean edge length, denoted  $\beta$ , averaged over numerically-generated networks. The set of points labelled  $\lambda = 0$  is generated according to the algorithm just described. The set of points labelled  $\lambda = 4$  is generated with the modification that, instead of connecting to the nearest available neighbour, vertices are connected to the  $j$ th nearest, where  $j-1$  is chosen from a Poisson distribution with mean  $\lambda$ . The data points were obtained by constructing networks with  $N$  between 100 and 40,000 in a sphere with radius 200  $\mu\text{m}$ . A practical consideration is the size of the computational domain, in particular the sorting required to establish connections during network generation which restricts the size of the computational domain. Domains of the size of a typical experimental imaging region inside a T cell zone are feasible, but models of an entire lymph node are not as yet feasible.

When the number of vertices,  $N$ , is sufficiently large, we observe that  $\beta = A(\lambda)\rho^{-1/3}$ , where we estimate  $A(\lambda) = 0.87 + 0.10\lambda$  from the data in Fig. 1. The deviation from  $\rho^{-1/3}$  scaling at low values of  $N$  is due to the increased proportion of vertices close to the surface of the sphere whose edges can only be with nodes in the interior. For example, the edge lengths of about 17  $\mu\text{m}$  that are estimated in mice lymph nodes (Bajénoff et al., 2006) are obtained with  $\rho \approx 10^5 \text{ mm}^{-3}$ , corresponding to 1000 per sphere of radius 133  $\mu\text{m}$ .

The probability density of the angle  $\theta$  between two edges sharing a vertex is shown in Fig. 2, for three values of  $\lambda$ . In each

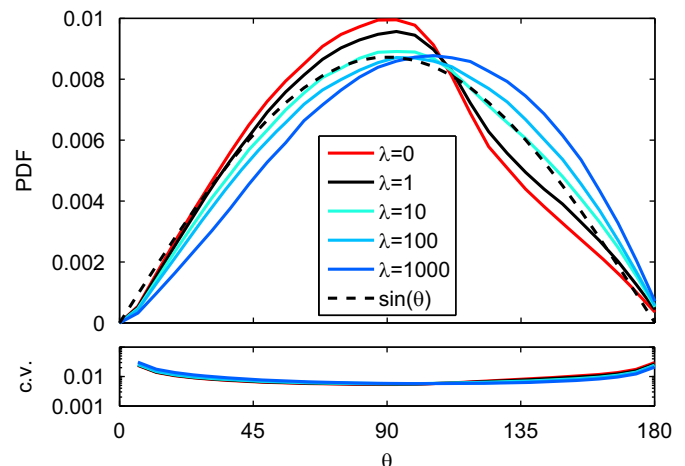


Fig. 2. Upper panel: probability densities (PDF) of angles between edges sharing a vertex, for  $\lambda$  ranging from 0 to 1000, sampled from 100 realisations with  $N=14,000$  and  $R=160 \mu\text{m}$ . The  $\sin \theta$  density is shown for comparison. Lower panel: corresponding coefficient of variation (c.v.) for each simulation.

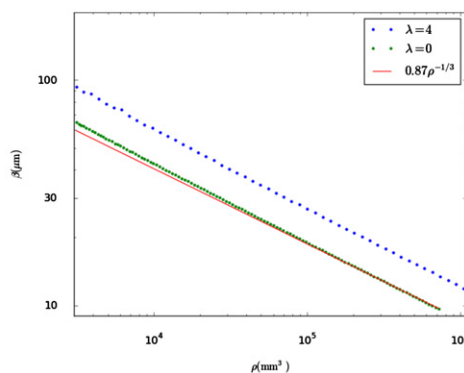


Fig. 1. Left: sample network.  $R=160 \mu\text{m}$ ,  $N=1000$  and  $\lambda=1$ . Right: mean edge length versus density of vertices, for random networks generated with  $R=200 \mu\text{m}$ . The solid line is  $\beta = 0.87\rho^{-1/3}$ .

case  $\beta \approx 17 \mu\text{m}$ , where  $N$  has been varied as necessary to preserve  $\beta$ . Symmetry around  $90^\circ$  would be found if successive edges were independent (Beltman et al., 2009). With our method of construction, turning angles smaller than  $90^\circ$  are slightly favoured with small values of  $\lambda$ . At sufficiently large values of  $\lambda$ , on the other hand, confinement of the nodes to a closed region produces an average turning angle close to  $120^\circ$ . We note that the distribution of edge turning angles is close to random only when the value of  $\lambda$  is in a relatively small range. Although it is not possible to assess which value of  $\lambda$  corresponds to real RN, we can conclude that the *in vivo* distribution of edge turning angles is unlikely to be symmetric about  $90^\circ$ .

In analysis of imaging data, turning angles are calculated from measurements of cell position at fixed time intervals. There are two consequences for the measured distribution of turning angles, compared to that of edge turning angles. First, a narrow peak at  $\theta = 0^\circ$  will appear, more prominent the smaller the time interval used, corresponding to cells that have remained on one edge for three or more timepoints. Second, the turning angle that is measured in the case where a cell does pass through a vertex to another edge will only correspond to the edge turning angle if the cell position is on the vertex at the second timepoint of three, otherwise the measured angle will be smaller than the edge turning angle.

## 2.2. Motion on the network

**Constant speed network motion (CSDB and CSNM):** A simple hypothesis is that cells travel at a constant speed changing direction upon reaching a vertex. At the vertex, an important distinction is made—between paths which are allowed to “double-back” onto the edge which they have just traversed, and those which must choose from the other edges. In each case, an edge is selected at random from those available. We refer to the former as constant speed network motion with doubling-back (CSDB) and the latter as constant speed network motion (CSNM). Each motion is thus characterised by the speed parameter denoted  $v$ . The speed is assumed constant at all times, including while turning onto a new edge. A movie illustrating CSDB is included as supplementary material.

Supplementary data associated with this article can be found in the online version of [10.1016/j.jtbi.2011.11.001](https://doi.org/10.1016/j.jtbi.2011.11.001).

As models for the movement of a T cell along an edge, the constant-speed and Brownian motion cases can be thought of as two ends of a spectrum of possibilities. At one end, the cell never changes direction, except perhaps at vertices; at the other end, the cell is constantly changing direction. For example, a cell that moves with constant speed  $v$ , and reverses its direction with constant probability,  $q$ , per unit time, will have mean-square displacement equal to  $2tv^2/q$  as  $t \rightarrow \infty$ . Models of stop-pause-go motion, for example, are used for the effective motion of T cells in three-dimensional space, resulting from motion along the network with branches (Beauchemin et al., 2007). It is to be expected that the characteristics of cell motion along an individual network edge *in vivo*, will be those of an intermediate case, with some of the characteristics of BNM and CSNM. It is also possible, of course, that cells could exhibit some more complex form of behaviour; for example, moving between nearby edges at locations not joined by a vertex.

It is also important to note that cells cannot exit the network, and thus over sufficiently long simulation times confinement effects appear. In order to minimise this, cells are started near the centre of the computational domain, and total simulation times are smaller than the mean time required to reach the boundary. A more detailed analysis of the effects of finite imaging volume can be found in Appendix A.

## 3. From network motion to apparent Brownian motion

We begin by recalling some properties of Brownian motion and of motion consisting of straight-line segments. Brownian motion in three space dimensions, with diffusivity  $D$ , is the stochastic process  $(\mathbf{X}_t, \mathbf{Y}_t, \mathbf{Z}_t)$  having independent Brownian motions, with diffusivity  $D$ , for each of its three Cartesian components (Ito and McKean, 1974; Stirzaker, 2005):

$$\mathbb{E}[\mathbf{X}_t^2] = \mathbb{E}[\mathbf{Y}_t^2] = \mathbb{E}[\mathbf{Z}_t^2] = 2Dt \quad \text{so} \quad \mathbb{E}[\mathbf{X}_t^2 + \mathbf{Y}_t^2 + \mathbf{Z}_t^2] = 6Dt.$$

The displacement at time  $t$ ,  $\mathbf{R}_t = (\mathbf{X}_t^2 + \mathbf{Y}_t^2 + \mathbf{Z}_t^2)^{1/2}$ , has mean  $\mathbb{E}[\mathbf{R}_t] = (16Dt/\pi)^{1/2}$ . Here, we measure the effective diffusivity of a T cell,  $D_{\text{eff}}$ , as the long-time limit of  $\mathbb{E}[\mathbf{X}_t^2 + \mathbf{Y}_t^2 + \mathbf{Z}_t^2]/6t$ .

If a T cell moves a distance  $l$  in a direction that is randomly-chosen in three space dimensions, then the mean-squared displacement in any one Cartesian direction is  $l^2/3$ . If the motion has constant speed  $v$  along each direction, then the time taken to traverse an edge with length  $l$  is  $l/v$ . The effective diffusivity of T cells following paths consisting of a succession of straight-line segments, each of length  $l$ , in independently-chosen directions is

$$D = \frac{\mathbb{E}[\mathbf{X}_t^2 + \mathbf{Y}_t^2 + \mathbf{Z}_t^2]}{6t} = \frac{l^2}{6l/v} = \frac{vl}{6}.$$

The “minimalist” model (Beauchemin et al., 2007) incorporates a pause time  $t_{\text{pause}}$  at each vertex, so that the total mean time to traverse an edge is  $l/v + t_{\text{pause}}$ , and  $D = (vl/6)(1 + vt_{\text{pause}}/l)^{-1}$ .

It is possible to modify the above “minimalist” model to take into account some of the features of motion on preformed networks. If the lengths  $l$  of the segments are not fixed, but themselves drawn independently from a probability density with  $\mathbb{E}[l] = \beta$  and  $\mathbb{E}[l^2] = \alpha$ , then

$$D = \frac{\alpha v}{\beta 6}. \quad (1)$$

For example, supposing that edge lengths vary between  $5 \mu\text{m}$  and  $37 \mu\text{m}$ , with mean  $17 \mu\text{m}$  (Beauchemin et al., 2007), a rough estimate based on a uniform distribution between  $5$  and  $29 \mu\text{m}$  gives  $\beta = 17 \mu\text{m}$  and  $\alpha = 337 \mu\text{m}^2$ . Then, for instance,  $v = 18 \mu\text{m}/\text{min}$  yields  $D \approx 59 (\mu\text{m})^2/\text{min}$ .

Second, the description can be modified by allowing the cell, with probability  $p$  at the end of each segment, to reverse its direction. Then the mean number of distinct segments traversed in time  $t$  is proportional to  $t(1-p)/(1+p)$  and

$$D = \frac{v\alpha(1-p)}{6\beta(1+p)}. \quad (2)$$

If all vertices are connected to three edges and a cell, once it arrives at a vertex, is allowed to take the edge along which it arrived, then  $p = \frac{1}{3}$  and so the factor  $(1-p)/(1+p)$  in (2) is precisely  $\frac{1}{2}$ .

Now consider motion in which a cell executes one-dimensional Brownian motion, with diffusivity  $D_{\text{lin}}$ , along an edge that is oriented in a randomly selected direction, until it has travelled a distance  $l$ , then in another direction, and so on. (Successive values of  $l$  may themselves be chosen from a probability density.) The mean time spent on an edge is  $l^2/2D_{\text{lin}}$ , and the relationship between the diffusivity of the motion on each edge, and the effective diffusivity is

$$D = \frac{\mathbb{E}[\mathbf{X}_t^2 + \mathbf{Y}_t^2 + \mathbf{Z}_t^2]}{6t} = \frac{l^2}{6} \frac{2D_{\text{lin}}}{l^2} = \frac{1}{3} D_{\text{lin}}. \quad (3)$$

On preformed networks, we observe effective diffusivities obeying this relationship if the rules for the choices of direction at vertices prevent the cell from revisiting an edge that has been traversed from end to end before another edge is traversed. The

property that the mean-square displacement is proportional to time is common to motions in which the number of distinct vertices visited in time  $t$  is proportional to  $t$ . An interesting counter-example, to be discussed in Section 4, where the number of distinct vertices visited and, consequently, the mean-squared displacement, are proportional to  $\sqrt{t}$ , is found for BNM.

In this section, we have derived formulae describing the apparent random motion that results from simple hypotheses about motion confined to a network. In the next, we consider the cell motion as observed in imaging experiments.

#### 4. Observed motion

Apparently random motion that results from motion along a preformed network is illustrated in Fig. 3. We followed individual T cells on a network for 12 min and imitated the experimental methodology of Miller et al. (2003) for analysing the motion of *in vivo* T cells as acquired by two-photon microscopy; that is, the three-dimensional cell traces are sampled every 10 s, projected into the two-dimensional  $x$ - $y$  plane, and adjusted to begin at the origin. The results are given as the individual traces, in the left panel, and mean displacement as a function of  $\sqrt{t}$ , in the right panel. As in Miller et al. (2002) (Fig. 3), Miller et al. (2003) (Fig. 4) and Mempel et al. (2004) (Fig. 1f), linear regression of the mean displacement versus  $\sqrt{t}$  is performed. Here we obtain a very good

linear fit with  $R^2 = 0.95$ . Equivalent simulations were performed for BNM; the results are given in Fig. 3D again with good linear fit; simulations for CSDB likewise yielded  $R^2 = 0.95$  (data not shown).

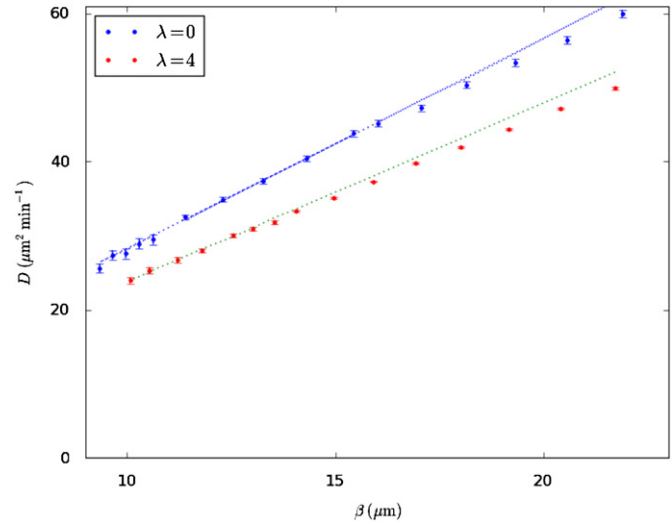


**Fig. 4.** Effective diffusivity versus mean edge length for CSDB with  $v = 12 \mu\text{m}/\text{min}$ . The solid lines are  $D_{\text{eff}} = (\alpha/\beta)v/6$ . The numerical realisations were carried out with  $R = 300 \mu\text{m}$ .

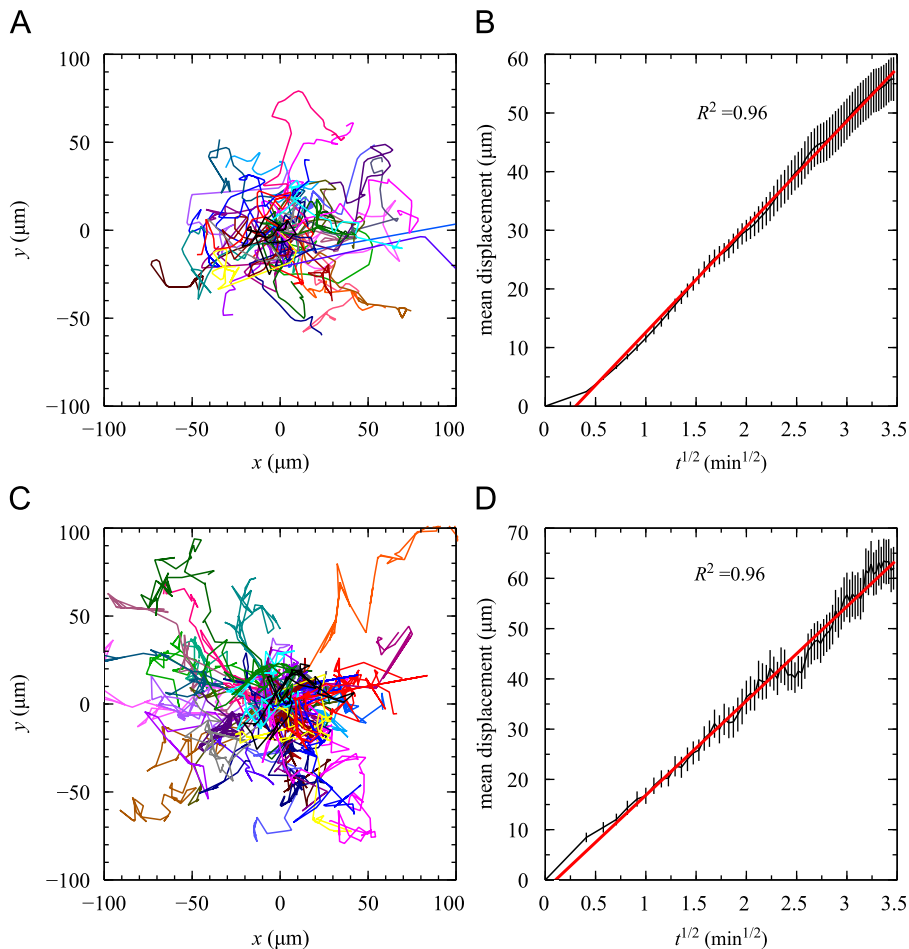


**Fig. 3.** (A and C): trajectories for 39 simulated cells undergoing (A) CSNM and (C) BNM on a network. The network contains  $N = 14,000$  nodes in a sphere of  $R = 160 \mu\text{m}$  using  $\lambda = 1$ , resulting in  $\beta = 17.47 \mu\text{m}$ . As in Miller et al. (2003), 39 cells are tracked for 12 min and observed six times per minute. (B and D): corresponding mean displacement, plotted as a function of  $\sqrt{t}$ , along with linear regression ( $R^2 = 0.96$ ). Standard error bars are given. In (B), CSNM with  $v = 20.45 \mu\text{m}/\text{min}$ , yielding an effective diffusivity of  $D_{\text{eff}} = 60 (\mu\text{m})^2/\text{min}$ . In (D), BNM with  $D_{\text{fm}} = 596.73 (\mu\text{m})^2/\text{min}$ .

4.1. Two regimes in mean displacement versus time

In the previous subsection, we have seen that different types of cell motion along edges, constant speed or Brownian may produce graphs of mean-squared displacement versus time that are constant slope over some time intervals. However, followed over longer times, differences emerge. If motion along edges is constant speed, the resemblance of paths to Brownian motion becomes stronger when cells are followed for longer times. In the case of BNM, however, the long-time behaviour is subdiffusive. In Fig. 4 we plot the effective diffusivity versus mean edge length for CSDB with  $v = 12 \mu\text{m}/\text{min}$ . The effective diffusivity, measure as described in Section 3, is well approximated by (1).

A persistent feature of plots of mean displacement versus  $\sqrt{t}$  for T cells, both in experimental and modelling studies, is that they exhibit two distinct scaling regimes: in the short-time regime, mean displacement is linear in  $t$  and is typically interpreted as an initial period of straight line, fixed speed movement; in the long-time regime mean displacement is linear in  $\sqrt{t}$  (i.e., Sumen and Mempel, 2004). This has been interpreted as a sort of persistence length, or mean free path, characterising the cell motion. In the context of movement on the network, there is an intuitive explanation: the first regime corresponds to movement along a single edge, and the second occurs as movement progresses across  $n$  edges, as  $n \rightarrow \infty$ .

It is easy to understand the initial, small-time regime for both BNM and CS motions. On a single edge, the displacement is on a line: CS motions move at a constant speed with displacement proportional to  $t$ ; BNM with mean displacement proportional to  $\sqrt{t}$ . The long-time regime has mean displacement growth in time which is the square root of the small-time regime. To understand this, consider the simple example of a non-intersecting path along a network, where all edges are of length  $l$  and successive directions are independently chosen at random—see Fig. 5. We first show by an induction argument that the following relationship holds between the number,  $n$ , of segments in random directions, and the distance,  $r_n$ , from the starting point, when the length of each segment is constant:

$$\mathbb{E}[r_n^2] = nl^2. \tag{4}$$

If  $n=1$ , the distance travelled is  $l$ , and the result holds. When  $n=2$ , the angle,  $\theta_1$ , between the first and second directions is symmetrically distributed about  $\theta_1 = \pi/2$ , so the mean distance is that found by averaging over all possible turning angles:  $\mathbb{E}[r_2^2] = 2l^2$ . Repeating this construction for two sides of a new triangle, now with one side of length  $\sqrt{(n-1)l^2}$  and the other of length  $l$ , yields (4). If the length of the path, up to time  $t$ , is  $l\eta(t)$  and the displacement at time  $t$  is  $r_{\eta(t)}$  then, for sufficiently small time, when  $\eta(t) < 1$ , the displacement is along a single edge, and

$$\sqrt{\mathbb{E}[r_{\eta(t)}^2]} = l\eta(t)$$

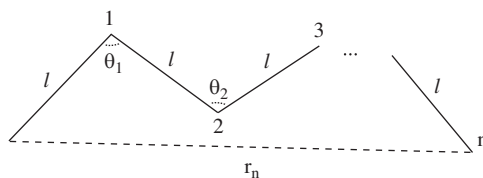


Fig. 5. Schematic illustrating geometric construction relating path length and displacement.

proportional to  $\eta(t)$ . For large time, when  $\eta(t) \gg 1$ , the path turns through many angles and, by (4),

$$\sqrt{\mathbb{E}[r_{\eta(t)}^2]} = l\sqrt{\eta(t)}$$

proportional to  $\sqrt{\eta(t)}$ .

In the case of CSNM  $\eta_{\text{CSNM}}(t) = vt/l$  and thus

$$\sqrt{\mathbb{E}[r_{\eta(t)}^2]} = \begin{cases} vt, & t \text{ small,} \\ \sqrt{lv}t, & t \text{ large.} \end{cases} \tag{5}$$

For BNM, on the other hand, the length along the path changes in time as  $\eta_{\text{BNM}}(t) = \sqrt{2D_{\text{lin}}t}/l$  and so

$$\sqrt{\mathbb{E}[r_{\eta(t)}^2]} = \begin{cases} \sqrt{2D_{\text{lin}}t}, & t \text{ small,} \\ (2D_{\text{lin}}l^2t)^{1/4}, & t \text{ large.} \end{cases} \tag{6}$$

The two-regime behaviour of CSNM and BNM motion is illustrated in Fig. 6. Note that a large value of  $\beta$  is chosen in order to visualise the small-time regime more clearly. In the case of CSNM, (A) and (B), the small-time behaviour is seen to be proportional to  $t$ , transitioning to diffusive,  $\propto \sqrt{t}$  behaviour for large times. In (C) and (D) simulation results are given for BNM with mean displacement plotted against  $\sqrt{t}$  and  $t^{1/4}$ . While the motion is initially linear in  $\sqrt{t}$ , for longer time it becomes linear in  $t^{1/4}$ , in agreement with (6). The dashed red lines are to aid the eye. In the same way that diffusive behaviour means that speed is not well-defined, long-time subdiffusive behaviour means that the diffusivity is, strictly speaking, zero.

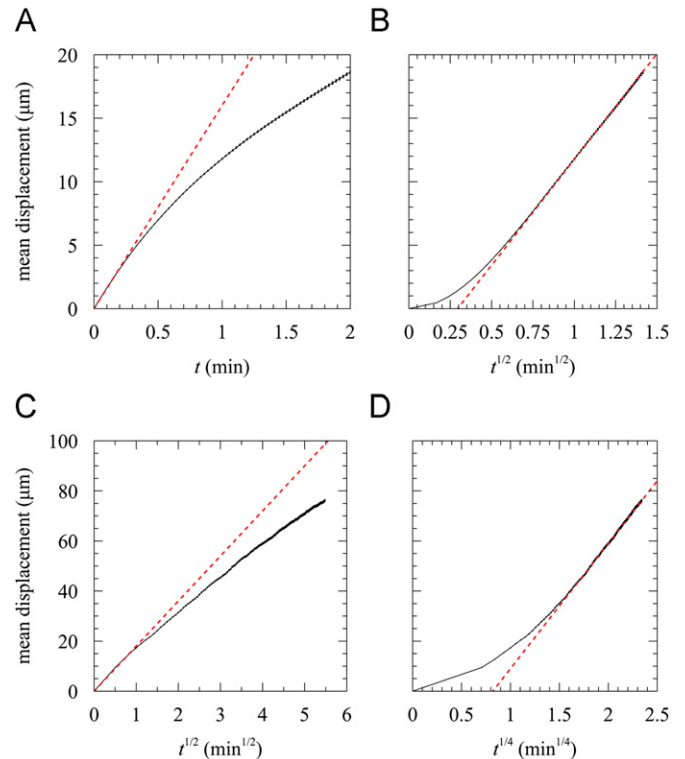
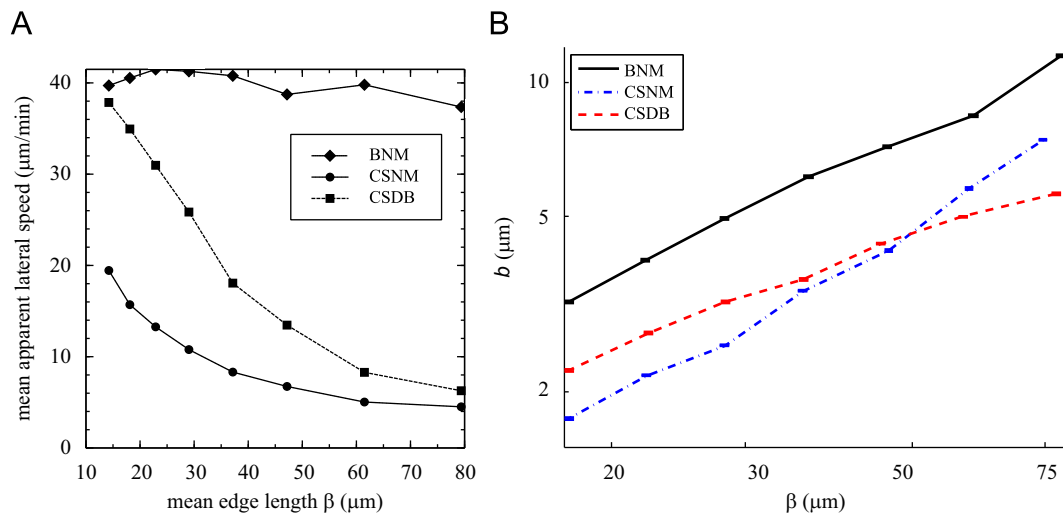


Fig. 6. Mean displacement collected from 3900 trajectories. (A and B): CSNM with  $v = 20.45 \mu\text{m}/\text{min}$ . (C and D): BNM with  $D_{\text{lin}} = 596.73 (\mu\text{m})^2/\text{min}$ . The networks used contained  $N = 14,000$  nodes within a radius  $R = 160 \mu\text{m}$  with  $\lambda = 1$ , resulting in mean edge length  $\beta = 17.47 \mu\text{m}$ . The mean displacement is plotted versus  $t$  in (A), and against  $\sqrt{t}$  in (B) and (C), and against  $t^{1/4}$  in (D), with dashed lines indicating approximate scaling regimes for small and large  $t$  (see text Section 4.1).



**Fig. 7.** (A) Mean apparent lateral speed for each type of motion, as measured by 50,000 Monte Carlo simulations, calculated from cell positions, at 10-s intervals, projected into the  $x$ - $y$  plane. (B) APC radii implied by mean cell collision time and (7). In each case,  $R = 160 \mu\text{m}$ ,  $\lambda = 1$  and  $v$  were chosen to obtain  $D_{\text{eff}} = 60 (\mu\text{m})^2/\text{min}$ .

#### 4.2. Apparent speed

One typical experimental measure of lymphocyte movement is the apparent speed, obtained by observing the position of the cell at a fixed observation frequency. Because experimental axial resolution is not as good as lateral resolution, lateral speeds are measured from point to point on tracks projected into the  $x$ - $y$  plane (Miller et al., 2003). In Fig. 7, we replicate the procedure of Miller et al. (2002, 2003, 2004a), by following cell motion over a 12 min period, making observations of position at 10 s intervals, and measuring the displacements in the  $x$ - $y$  plane. These displacements are then divided by the observation period to give an apparent lateral speed. The mean speed is given as a function of mean edge length  $\beta$ . At each value of  $\beta$ , the constant speed  $v$  is chosen so that  $D_{\text{eff}} = 60 \pm 1.2 (\mu\text{m})^2/\text{min}$ . As may be expected from (1) and (2), the value of  $v$  needed to yield a given value of  $D_{\text{eff}}$  with CSDB motion is twice that required with CSNM. Mean apparent lateral speed measurements reported in the literature are near  $10 \mu\text{m}/\text{min}$  (Miller et al., 2002); comparison with Fig. 7 suggests that the results from CSNM are closest to experimental values. The mean apparent lateral speeds obtained from measurements of BNM taken at time intervals separated by  $\Delta t$  are proportional to  $(\Delta t)^{-1/2}$ . If  $D_{\text{eff}} = 60 (\mu\text{m})^2/\text{min}$  then apparent velocities of order  $10 \mu\text{m}$  will be found over time intervals of about 1 min; smaller  $\Delta t$  yields larger apparent velocities.

In summary, in this section we have shown how T cell motion restricted to a preformed network would manifest itself in the methodology typically used to analyse data from two-photon imaging of lymph nodes *in vivo*. The simplest type of motion, where velocity is constant along edges, is consistent with current experimental data and has effective diffusivity well-approximated by a simple formula. BNM, or motion with multiple changes of direction along an edge, will be subdiffusive if observed for sufficiently long times.

#### 5. Cell collisions

The underlying immunological question of cell dynamics in lymph nodes is that of collision times—how long does it take for an APC to come in contact with a specific T cell? We compare mean collision times, when cell movement is restricted to a

network of vertices and edges, with those from off-network motion. Note that, on a network, modelling cells as point particles is sufficient to obtain collisions. In contrast, to obtain collisions between cells moving in three spatial dimensions, at least one of the cell types must have a non-zero radius of attraction because point particles moving independently in three space dimensions do not collide.

Here we choose to compare the rates of collision in network and off-network models by fixing the effective diffusivity, measuring the rate of collision on a computational network, and calculating the effective radius that would need to be assumed in an off-network Brownian motion model to obtain the same rate of collision. That is, for any given network size and fixed  $D_{\text{eff}}$ , the resulting mean collision time for network-based motion implies an effective cell radius: the cell radius for off-network motion which yields the same mean collision time.

In each numerical realisation, one T cell and one APC are given random initial conditions on the network; the T cell moves according to the rules of motion until colliding with the stationary APC. Before each numerical evaluation of the frequency of collisions on a network, we establish the values of the motion parameters ( $D_{\text{lin}}$  or  $v$ ) by Monte Carlo simulation (50,000 trials) over a fixed time period (12 min).

The mean time for collision between a T cell (assumed to be a point-particle) moving according to Brownian motion with diffusivity  $D_{\text{eff}}$  in a sphere of radius  $R$ , and a stationary APC with finite radius  $b$ , is (Redner, 2001)

$$\tau = \frac{R^3}{3bD_{\text{eff}}}. \quad (7)$$

The mean collision time  $\tau$  can be calculated for network-based motions by Monte Carlo simulation, thus allowing a calculation of the implied APC radius,  $b$ . Results are given in Fig. 7, panel B, where each simulation data point is obtained from 50,000 Monte Carlo simulations with  $R = 160 \mu\text{m}$  and  $D_{\text{eff}} = 60 (\mu\text{m})^2/\text{min}$ . For each type of motion as the mean edge length  $\beta$  decreases so does the implied APC radius. This corresponds to an increase in the mean collision time, which arises from an increase in total network size. The T cell must search a larger and larger network as  $\beta$  decreases, resulting in increased collision times.

The mean collision time is observed to be proportional to the sum of the lengths of all the edges,  $N\beta$ , which is proportional to  $\rho^{2/3}$ .

We find

$$\tau = \frac{R^3}{kv\beta^2}, \quad (8)$$

where we estimate  $k=0.0439$  for CSNM and  $k=0.0200$  for CSDB.

In the estimated physiological range of  $\beta$  of 5–37  $\mu\text{m}$  (Bajénoff et al., 2006), implied APC radii under network-based motion are thus smaller than effective APC radii of approximately 19  $\mu\text{m}$  (Miller et al., 2004a). (In three-dimensional collision models, the radius of attraction may in fact be larger than the physical cell radius, due to local chemical signalling and dendritic APC structure (Day and Lythe, 2011).) In this sense, there is no increase in contact efficiency due to RN-based motion.

## 6. Discussion

We construct an explicit network within the lymph node using an algorithm for generating random spatial networks. Network motion is an attractive hypothesis because it is able to produce linear motion at short timescales and apparent Brownian motion at longer timescales. The simplest, constant speed, motions reproduce this characteristic two-regime behaviour with mean displacement as a function of time initially proportional to time and later proportional to the square root of time. The effective diffusivity is approximately  $\alpha/\beta v/6$ , where  $\beta$  is the mean edge length and  $\alpha$  is the mean-square edge length. Allowing a cell to reverse direction at a vertex reduces its  $D_{\text{eff}}$  by a factor of 2. If the motion along edges is itself Brownian then the resulting cell path is subdiffusive.

The distribution of cell turning angles depends, under the assumption that cell motion is confined to the RN, on the distribution of network edge turning angles. In our numerically-constructed networks it is unusual to find a distribution of edge turning angles that are random. We conclude that it should be possible to observe the non-random distribution of turning angles in analysis of *in vivo* imaging data as a consequence of network motion. Of course, such bias in the turning angle distribution could also be a result of a different type of persistent motion.

One possible rationale for the hypothesis of network-based motion is that physical contacts between cells, such as an APC and T cell, can be arranged more efficiently on the network than if all cells wander freely in space. This was examined in Section 5 by calculating the implied effective APC radius for each type of motion. However, the implied APC radii are not sufficiently large to justify the hypothesis that network motion, by itself, increases the efficiency of cell collisions when compared with off-network Brownian motion.

From the point of view of collision times, lower-density networks are more efficient. However, a dense network would be required to sustain the hypothesis that most T cells, even in a crowded lymph node, are constrained to move along it. Note that, in our network dynamics model, however, we have not included the possible effects of chemical gradients and occasional off-network motion that may result in improved contact efficiency (Mempel et al., 2006; Bajénoff et al., 2008).

Choices have been made in this work in the construction of networks, for example that each vertex is connected to exactly three edges. This assumption was motivated both by the idea that the network is formed by branching, and by the micrographs of Ushiki et al. (1995), which show almost exclusively connections of this type. Our model could be modified to allow for the possibility of more than three edges at a vertex, to remove long edges, or to incorporate curved edges. It would also be interesting to consider algorithms that "grow" a network, beginning from a single node and propagating outwards, although they tend to

produce a tree-like structure and contain a few long edges that can have an important influence (Callaway et al., 2001). The networks considered here also contain a small number of long edges, due to the nature of the generation algorithm; the influence of these links, and their relationship to the properties of the genuine physiological network, is an important area for future work.

If T cells routinely follow the FRC network, rather than exploring the full three-dimensional volume available to them in the T cell zone of a lymph node, then T cells will be found in the same location at different times. Recent multiphoton observations of lymphocyte motion have revealed evidence that changes in T cell direction coincide with branches of the network (Bajénoff et al., 2006, 2008; Sanos et al., 2011). On the other hand, our result that the rate of encounters between cells is not enhanced under the assumption that cells always move on a dense network, and the question of how simultaneous motion of many cells could be arranged under this assumption, suggest that a modified model where cells occasionally leave the network, is a fruitful area for study. It may also be possible for the current generation of imaging experiments to yield precise data, on the distribution of edge lengths *in vivo* and on cell motion along individual edges, that can be used to refine computational models such as that introduced here.

## Acknowledgements

This work arose from a collaborative visit held under the auspices of the FP7 IRSES *International Network on Theoretical Immunology*.

## Appendix A. Finite volume effects

Both in this modelling study, and in the experiments with which we compare, lymphocytes are not imaged as they move freely throughout the entire lymph node, but are instead confined to a smaller imaging region. For example, Miller et al. (2002) image a  $200 \times 200 \times 50 \mu\text{m}^3$  region, while we have considered a sphere with radius 160  $\mu\text{m}$  (except where explicitly varied). Because these regions are artificial, it is important to consider the implications of this finite domain size.

We begin by reconsidering the mean displacement versus  $\sqrt{t}$  for smaller imaging regions, centered within the  $R=160 \mu\text{m}$  sphere. Now, if a particle track exits the imaging region, that is treated as the end of the track (i.e., the particle has been lost). If it subsequently re-enters the imaging region, it is treated as a new track. We consider imaging regions of  $100 \times 100 \times 25 \mu\text{m}^3$  and  $50 \times 50 \times 12.5 \mu\text{m}^3$  with particles tracked for 12 min. The resulting mean displacements are given in the left panel of Fig. A1, along with the results in the sphere for comparison. At  $100 \times 100 \times 25 \mu\text{m}^3$ , the particles exhibit mild confinement within 12 min, with the mean displacement drifting below the target value during the latter stages of the simulation. At  $50 \times 50 \times 12.5 \mu\text{m}^3$ , the particles are severely confined, with a significant reduction in the final mean displacement. Although our computational domain is insufficiently large to perform the same experiment with the full  $200 \times 200 \times 50 \mu\text{m}^3$  region, extrapolating from the smaller imaging regions clearly suggests that over a 12 min observation period, confinement effects would not be significant in a domain of that size.

To quantify this confinement effect more fully, we vary both the simulation time and  $R$  with  $v$  fixed under CSNM. We then measure  $D_{\text{eff}}$  (the mean slope of the mean displacement versus  $\sqrt{t}$  curve). The value  $v=23 \mu\text{m}/\text{min}$  is chosen to give

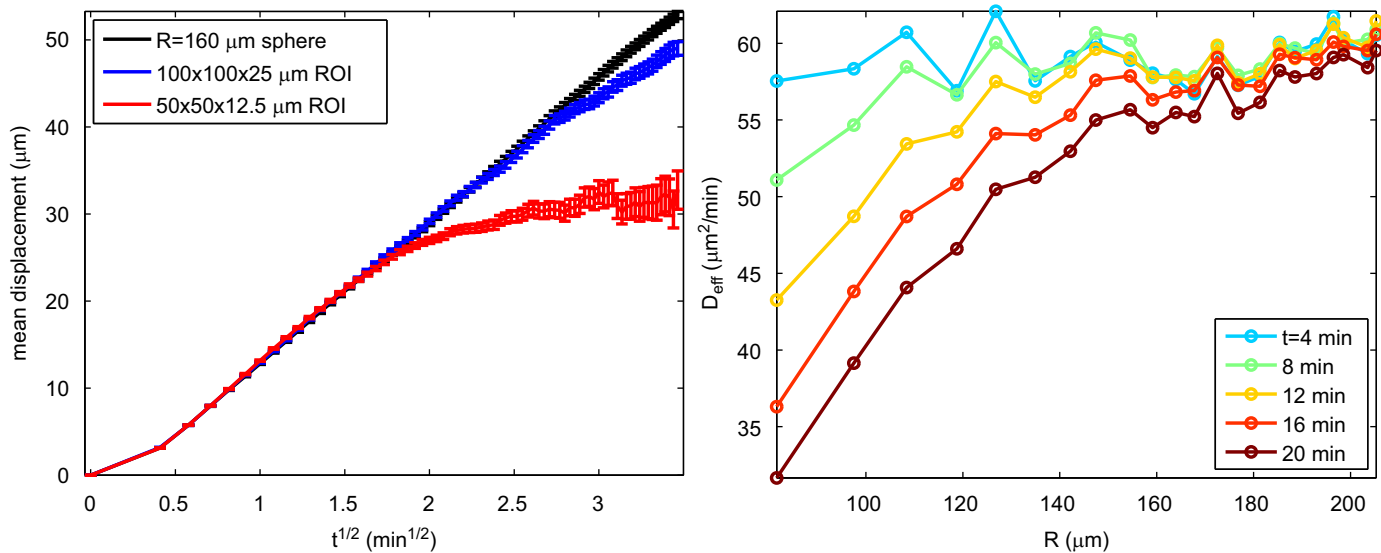


**Fig. A1.** Effects of finite volume. Left panel: mean displacement versus  $\sqrt{t}$  for increasingly confined imaging regions. As the ROI becomes smaller, the maximum possible mean displacement also decreases. Right panel: quantifying confinement varying both time and  $R$ . Here CSNM motion is considered with  $\beta = 17 \mu\text{m}$ , and  $v = 23 \mu\text{m}/\text{min}$  chosen to yield  $D_{\text{eff}} \approx 60 (\mu\text{m})^2/\text{min}$  in unconfined simulations; values significantly below this indicate simulations confined by the finite volume.

$D_{\text{eff}} \approx 60 (\mu\text{m})^2/\text{min}$  in unconfined situations; confinement is then indicated by  $D_{\text{eff}} < 60 (\mu\text{m})^2/\text{min}$ . Simulations are performed varying the duration from 4 to 20 min, and  $R$  from 80 to 200  $\mu\text{m}$ , with the results given in the right panel of Fig. A1. For severely confined simulations (long time and small  $R$ ),  $D_{\text{eff}}$  values are decreased by nearly a factor of 2 indicating severe confinement. However, for the values used elsewhere in this manuscript ( $t = 12 \text{ min}$ ,  $R = 160 \mu\text{m}$ ) or better, confinement effects are negligible.

## References

- Bajénoff, M., Egen, J., Koo, L., Laugier, J., Brau, F., Glaichenhaus, N., Germain, R., 2006. Stromal cell networks regulate lymphocyte entry, migration, and territoriality in lymph nodes. *Immunity* 25, 989–1001.
- Bajénoff, M., Egen, J., Qi, H., Huang, A., Castellino, F., Germain, R., 2007. Highways, byways and breadcrumbs: directing lymphocyte traffic in the lymph node. *Trends Immunol.* 28, 346–352.
- Bajénoff, M., Glaichenhaus, N., Germain, R., 2008. Fibroblastic reticular cells guide T lymphocyte entry into and migration within the splenic T cell zone. *J. Immunol.* 181, 3947.
- Beauchemin, C., Dixit, N., Perelson, A., 2007. Characterizing T cell movement within lymph nodes in the absence of antigen. *J. Immunol.* 178, 5505.
- Beltman, J., Marée, A., de Boer, R., 2009. Analysing immune cell migration. *Nat. Rev. Immunol.* 9, 789–798.
- Beltman, J., Maree, A., Lynch, J., Miller, M., de Boer, R., 2007a. Lymph node topology dictates T cell migration behavior. *J. Exp. Med.* 204, 771.
- Beltman, J.B., Maree, A.F.M., de Boer, R.J., 2007b. Spatial modelling of brief and long interactions between T cells and dendritic cells. *Immunol. Cell Biol.* 85, 306–314.
- Bogle, G., Dunbar, P., 2008. Simulating T-cell motility in the lymph node paracortex with a packed lattice geometry. *Immunol. Cell Biol.* 86, 676–687.
- Bouso, P., 2008. T-cell activation by dendritic cells in the lymph node: lessons from the movies. *Nat. Rev. Immunol.* 8, 675–684.
- Bouso, P., Bhakta, N., Lewis, R., Robey, E., 2002. Dynamics of thymocyte-stromal cell interactions visualized by two-photon microscopy. *Science* 296, 1876–1880.
- Callaway, D., Hopcroft, J., Kleinberg, J., Newman, M., Strogatz, S., 2001. Are randomly grown graphs really random? *Phys. Rev. E* 64, 41902.
- Catron, D., Itano, A., Pape, K., Mueller, D., Jenkins, M., 2004. Visualizing the first 50 hr of the primary immune response to a soluble antigen. *Immunity* 21, 341–347.
- Celli, S., Garcia, Z., Bouso, P., 2005. CD4 T cells integrate signals delivered during successive DC encounters in vivo. *J. Exp. Med.* 202, 1271–1278.
- Charnick, S., Lauffenburger, D., 1990. Mathematical analysis of cell-target encounter rates in three dimensions. Effect of chemotaxis. *Biophys. J.* 57, 1009–1023.
- Day, M., Lythe, G., 2011. Timescales of the adaptive immune response. In: Molina-París, C., Lythe, G. (Eds.), *Mathematical Models and Immune Cell Biology*, Springer.
- Deijfen, M., 2009. Stationary random graphs with prescribed iid degrees on a spatial poisson process. *Electron. Commun. Probab.* 14, 81–89.
- Garside, P., Brewer, J., 2008. Real-time imaging of the cellular interactions underlying tolerance, priming, and responses to infection. *Immunol. Rev.* 221, 130.
- Gretz, J., Anderson, A., Shaw, S., 1997. Cords, channels, corridors and conduits: critical architectural elements facilitating cell interactions in the lymph node cortex. *Immunol. Rev.* 156, 11–24.
- Grigorova, I., Pantelev, M., Cyster, J., 2010. Lymph node cortical sinus organization and relationship to lymphocyte egress dynamics and antigen exposure. *Proc. Natl. Acad. Sci.* 107, 20447.
- Holroyd, A., Pemantle, R., Peres, Y., Schramm, O., 2009. Poisson matching. *Ann. Inst. Henri Poincaré, Probab. Stat.* 45, 266–287.
- Hugues, S., Fetler, L., Bonifaz, L., Helft, J., Amblard, F., Amigorena, S., 2004. Distinct T cell dynamics in lymph nodes during the induction of tolerance and immunity. *Nat. Immunol.* 5, 1235–1242.
- Ito, K., McKean Jr., H., 1974. *Diffusion Processes and their Sample Paths*. Springer.
- Kaldjian, E., Gretz, J., Anderson, A., Shi, Y., Shaw, S., 2001. Spatial and molecular organization of lymph node T cell cortex: a labyrinthine cavity bounded by an epithelium-like monolayer of fibroblastic reticular cells anchored to basement membrane-like extracellular matrix. *Int. Immunol.* 13, 1243.
- Katakai, T., Hara, T., Sugai, M., Gonda, H., Shimizu, A., 2004. Lymph node fibroblastic reticular cells construct the stromal reticulum via contact with lymphocytes. *J. Exp. Med.* 200, 783.
- Lämmermann, T., Sixt, M., 2008. The microanatomy of T-cell responses. *Immunol. Rev.* 221, 26–43.
- Link, A., Vogt, T., Favre, S., Britschgi, M., Acha-Orbea, H., Hinz, B., Cyster, J., Luther, S., 2007. Fibroblastic reticular cells in lymph nodes regulate the homeostasis of naive T cells. *Nat. Immunol.* 8, 1255–1265.
- Mempel, T., Henrickson, S., Von Andrian, U., 2004. T-cell priming by dendritic cells in lymph nodes occurs in three distinct phases. *Nature* 427, 154–159.
- Mempel, T., Junt, T., von Andrian, U., 2006. Rulers over randomness: stroma cells guide lymphocyte migration in lymph nodes. *Immunity* 25, 867–869.
- Meyer-Hermann, M., Maini, P., 2005. Interpreting two-photon imaging data of lymphocyte motility. *Phys. Rev. E* 71, 61912.
- Miller, M., Hejazi, A., Wei, S., Cahalan, M., Parker, I., 2004a. T cell repertoire scanning is promoted by dynamic dendritic cell behavior and random T cell motility in the lymph node. *Proc. Natl. Acad. Sci.* 101, 998–1003.
- Miller, M., Safrina, O., Parker, I., Cahalan, M., 2004b. Imaging the single cell dynamics of CD4<sup>+</sup> T cell activation by dendritic cells in lymph nodes. *J. Exp. Med.* 200, 847.
- Miller, M., Wei, S., Parker, I., Cahalan, M., 2002. Two-photon imaging of lymphocyte motility and antigen response in intact lymph node. *Science* 296, 1869–1873.
- Miller, M.J., Wei, S.H., Cahalan, M.D., Parker, I., 2003. Autonomous T cell trafficking examined in vivo with intravital two-photon microscopy. *Proc. Natl. Acad. Sci. USA* 100, 2604–2609.
- Millington, O., Zinselmeyer, B., Brewer, J., Garside, P., Rush, C., 2007. Lymphocyte tracking and interactions in secondary lymphoid organs. *Inflamm. Res.* 56, 391–401.
- Mueller, S., Ahmed, R., 2008. Lymphoid stroma in the initiation and control of immune responses. *Immunol. Rev.* 224, 284–294.
- Mueller, S., Germain, R., 2009. Stromal cell contributions to the homeostasis and functionality of the immune system. *Nat. Rev. Immunol.* 9, 618–629.

- Preston, S.P., Waters, S.L., Jensen, O.E., Heaton, P.R., Pritchard, D.I., 2006. T-cell motility in the early stages of the immune response modeled as a random walk amongst targets. *Phys. Rev. E* 74, 011910.
- Redner, S., 2001. *A Guide to First-passage Processes*. Cambridge University Press.
- Riggs, T., Walts, A., Perry, N., Bickle, L., Lynch, J., Myers, A., Flynn, J., Linderman, J., Miller, M., Kirschner, D., 2008. A comparison of random vs. chemotaxis-driven contacts of T cells with dendritic cells during repertoire scanning. *J. Theor. Biol.* 250, 732–751.
- Sanos, S., Nowak, J., Fallet, M., Bajenoff, M., 2011. Stromal cell networks regulate thymocyte migration and dendritic cell behavior in the thymus. *J. Immunol.* 64.
- Sixt, M., Kanazawa, N., Selg, M., Samson, T., Roos, G., Reinhardt, D., Pabst, R., Lutz, M., Sorokin, L., 2005. The conduit system transports soluble antigens from the afferent lymph to resident dendritic cells in the T cell area of the lymph node. *Immunity* 22, 19–29.
- Stirzaker, D., 2005. *Stochastic Processes and Models*. Oxford University Press.
- Stoll, S., Delon, J., Brotz, T., Germain, R., 2002. Dynamic imaging of T cell-dendritic cell interactions in lymph nodes. *Science* 296, 1873–1876.
- Sumen, C., Mempel, T., 2004. Intravital microscopy: visualizing immunity in context. *Immunity* 21, 315–329.
- Textor, J., Peixoto, A., Henrickson, S., Sinn, M., von Andrian, U., Westermann, J., 2011. Defining the quantitative limits of intravital two-photon lymphocyte tracking. *Proc. Natl. Acad. Sci.*
- Ushiki, T., Ohtani, O., Abe, K., 1995. Scanning electron microscopic studies of reticular framework in the rat mesenteric lymph node. *Anat. Rec.* 241, 113–122.
- Wei, S., Parker, I., Miller, M., Cahalan, M., 2003. A stochastic view of lymphocyte motility and trafficking within the lymph node. *Immunol. Rev.* 195, 136–159.
- Woolf, E., Grigorova, I., Sagiv, A., Grabovsky, V., Feigelson, S., Shulman, Z., Hartmann, T., Sixt, M., Cyster, J., Alon, R., 2007. Lymph node chemokines promote sustained T lymphocyte motility without triggering stable integrin adhesiveness in the absence of shear forces. *Nat. Immunol.* 8, 1076–1085.
- Worbs, T., Förster, R., 2009. T cell migration dynamics within lymph nodes during steady state: an overview of extracellular and intracellular factors influencing the basal intranodal T cell motility. In: *Visualizing Immunity*, Springer, pp. 71–105.
- Zinselmeyer, B., Dempster, J., Gurney, A.M., Wokosin, D., Miller, M., Ho, H., Millington, O.R., Smith, K.M., Rush, C.M., Parker, I., Cahalan, M., Brewer, J.M., Garside, P., 2005. In situ characterization of CD4<sup>+</sup> T cell behavior in mucosal and systemic lymphoid tissues during the induction of oral priming and tolerance. *J. Exp. Med.* 201, 1815–1823.